Supporting Information For:

Development of a spin selective electrocatalyst platform and its use to study spin-polarization and d-orbital occupancy effects in oxygen evolution reaction electrocatalysts.

*Meera Joy,[1] Brian P. Bloom,[1] Keerthana Govindaraj,[1] Joseph A. Albro,[1] Aravind Vadakkayil,[1] David H. Waldeck[1]**

[1] Chemistry Department, University of Pittsburgh, Pittsburgh, Pennsylvania 15260, United States

Figure S1 shows the characterization of the grafted substrates. Panel **a** shows an AFM topography image of a PANI film. Here, a 1 μm^2 region of the the grafted film was removed via scratching using an AFM tip in contact mode with an applied force of approximately 50 nN to reveal the underlying substrate. After scratching a subsequent noncontact mode imaging scan was taken of the scratched region and surrounding grafted film. The line averaged profile was taken from the topography image from the area highlighted in red in the topography. The averages of the data from the region with grafted layer and the region with the exposed substrate are plotted as a height profile below with the teal dashed lines indicating the difference in height between the two regions (c.a. 2 ± 0.7 nm). Panel **b** shows cyclic voltammetry measurements made with a solution of 5 mM p-phenylene diamine, and 1 equivalent of sodium nitrite in 0.5 M HCl. The reduction peak at -0.4 V versus Ag/AgCl reflects covalent attachment of the *in situ* generated diazoinum salt onto the electrode. Disappearance of the peak in the second cycle of the voltammogram indicates complete passivation of the surface after electrografting; consistent with that shown in other works.[1]

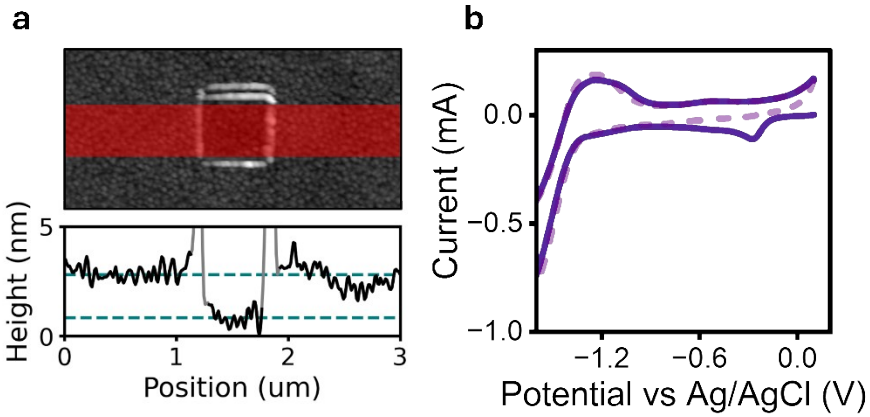

Figure S1. (**a**) AFM-based height measurement of a grafted sample. (**b**) Cyclic voltammetry for grafting process through reduction of *in situ* generated diazonium salt.

Figure S2 shows a thickness calibration plot for the polyaniline films. Panel a shows a series of absorbance spectra collected for films prepared with different polymerization times; the red arrow indicates increasing polymerization time. Panel b plots the maximum absorbance at ~340 nm against the thickness of the film that was measured by profilometry at 5 different spots in the film.

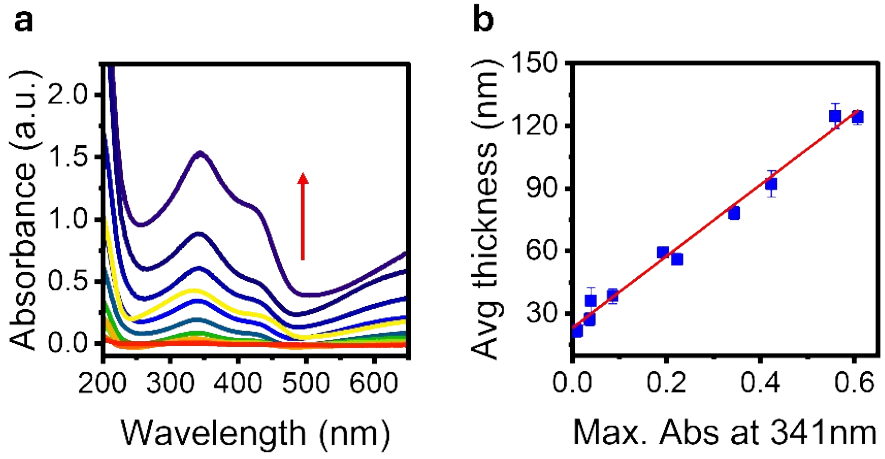

Figure S2. (**a**) UV-Vis absorbance of a series of polyaniline films prepared with different polymerization times is shown. The red arrow indicates increasing polymerization time. (**b**) Thickness calibration curve between the absorbance at 341 nm and the thickness of the film determined using a surface profilometer.

To quantify the spin polarization properties of PANI, mc-AFM measurements were performed. **Figures S3 a-c** show mc-AFM measurements for S-, R- and rac-PANI films, respectively, with a North and South magnetized tip. For S-PANI films, a higher current is observed with a South magnetized tip (spins aligned antiparallel to the momentum of electron) and a lower current is observed with a North magnetized tip (spins aligned parallel to the momentum of electron). Conversely, an opposite response was observed for R-PANI; a higher current is observed for spins aligned antiparallel to their momentum than parallel. For rac-PANI films no difference in *I-V* characteristics with tip magnetization was observed.

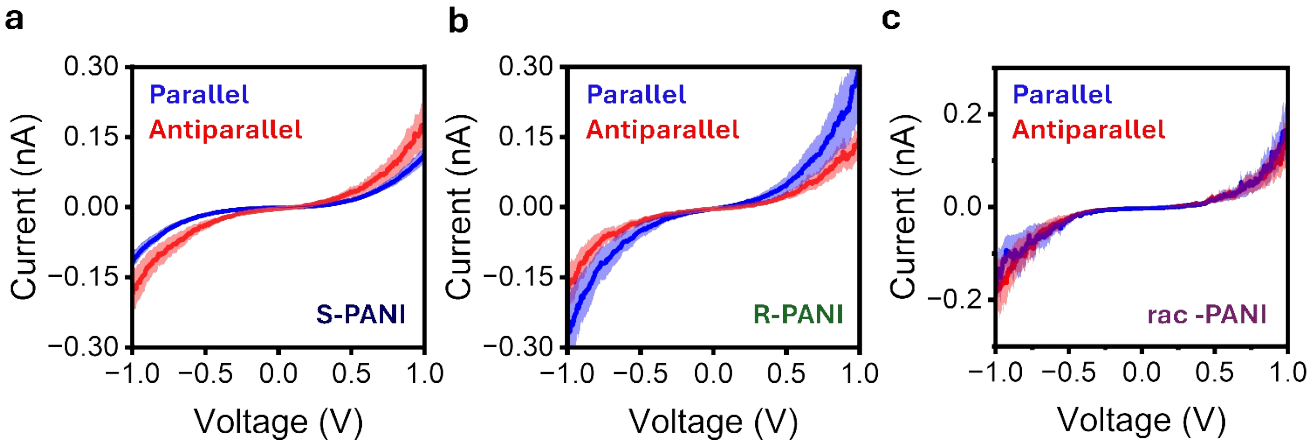

Figure S3. mcAFM measurements are shown for (**a**) S-PANI, (**b**) R-PANI, and (**c**) rac-PANI films in which the electron spin is aligned parallel (blue) or antiparallel (red) to its momentum. The solid line corresponds to the average *I-V* response and the shaded regions correspond to the 95% confidence intervals.

Figure S4 shows circular dichroism spectra of S- (blue), R- (green), and rac- (purple) PANI, following electrodeposition of nickel (**a**), iron (**b**), cobalt (**c**) and copper (**d**) catalysts. The mirror image CD response for the S-PANI and R-PANI catalyst supports is associated with spectral signatures of the PANI and not those of the electrodeposited catalyst. These studies imply that electrodeposition does not destroy the chiality of the underlying

PANI layer. Note that, electrodeposition was performed at reducing potentials which change the oxidation state of PANI to the completely reduced leucoemeraldine state,[2] and this change is responsible for the difference in features compared to that shown in Figure 1.

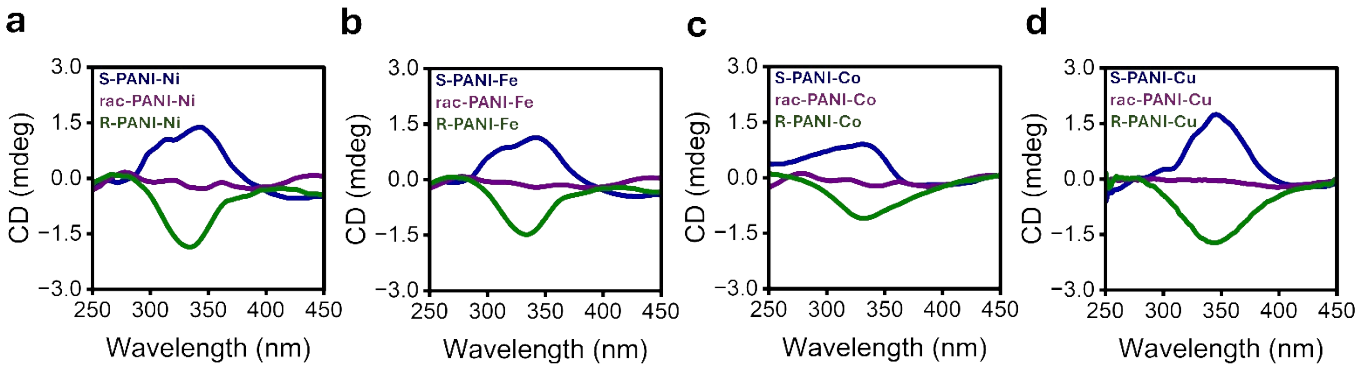

Figure S4. Circular dichroism spectra of S- (blue), R- (green), and rac- (purple) PANI films following electrodeposition of nickel (**a**), iron (**b**), cobalt (**c**), and copper (**d**) catalysts.

Figure **S5** shows high resolution Ni2p, Fe2p, Co2p, and Cu2p, XPS data for Ni (**a**), Fe (**b**), Co (**c**), and Cu (**d**) catalysts on R-PANI (bottom), S-PANI (middlde), and rac-PANI (top) coated electrodes. The red dashed line indicates that the binding energies for the Ni2p3/2, Fe2p3/2, Co2p3/2, and Cu2p3/2 peaks are similar when deposited on the different forms of PANI. Note that, the existance of multiple oxide, hydroxide, and oxyhydroxide forms of a given transition metal makes deconvolution complicated and in some instances unrealistic. Because the catalysts begin as electrodeposited metals, one would have to consider all possible oxidized forms in the fitting for accuracy; i.e. for cobalt this would entail fitting the Co2p spectra to a sum of >20 peaks,[2] a process that cannot be performed accurately. Instead of defining the particular form of the catalyst prior to OER, we emphasize the similarity between the chiral catalysts to that of the racemic catalysts to demonstrate that catalyst commposition is not responsible for the observed differences in activity. Figure **S6** plots the difference in normalized counts, to the peak maximum of the most intense peak, of chiral to racemic PANI-catalysts for each system. The top panel shows the maximum possible difference of the normalized spectra and the bottom panel zooms in five times. Note, the red dashed line is plotted at $\Delta=0$ as a guide. For some systems (e.g. Cu and Ni) slight differences in the $2p_{3/2}$ and $2p_{1/2}$ FWHM between chiral PANI and racemic PANI are observed, however this likely arises from spot-to-spot variations in roughness or surface charging during data acquisition. It is crucial to emphasize that no new peaks emerge and no deviations in baseline occur in the difference spectra which imply that the composition of the catalysts are the same when deposited on rac-PANI, S-PANI, and R-PANI.

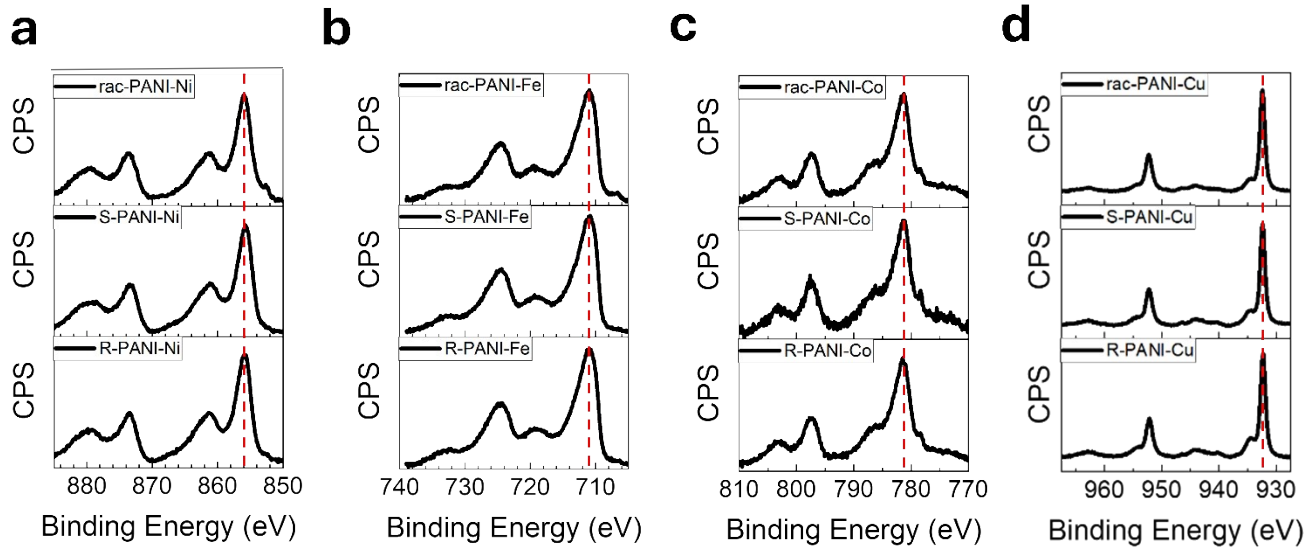

Figure S5. Panels (**a**), (**b**), (**c**), and (**d**) show high resolution Ni2p, Fe2p, Co2p, and Cu2p XPS spectra of rac- (top), S- (middle), and R-PANI (bottom) respectively. The red dashed line shows that the binding energy of the main peak in each spectrum occurs at a similar binding energy for the different forms of PANI.

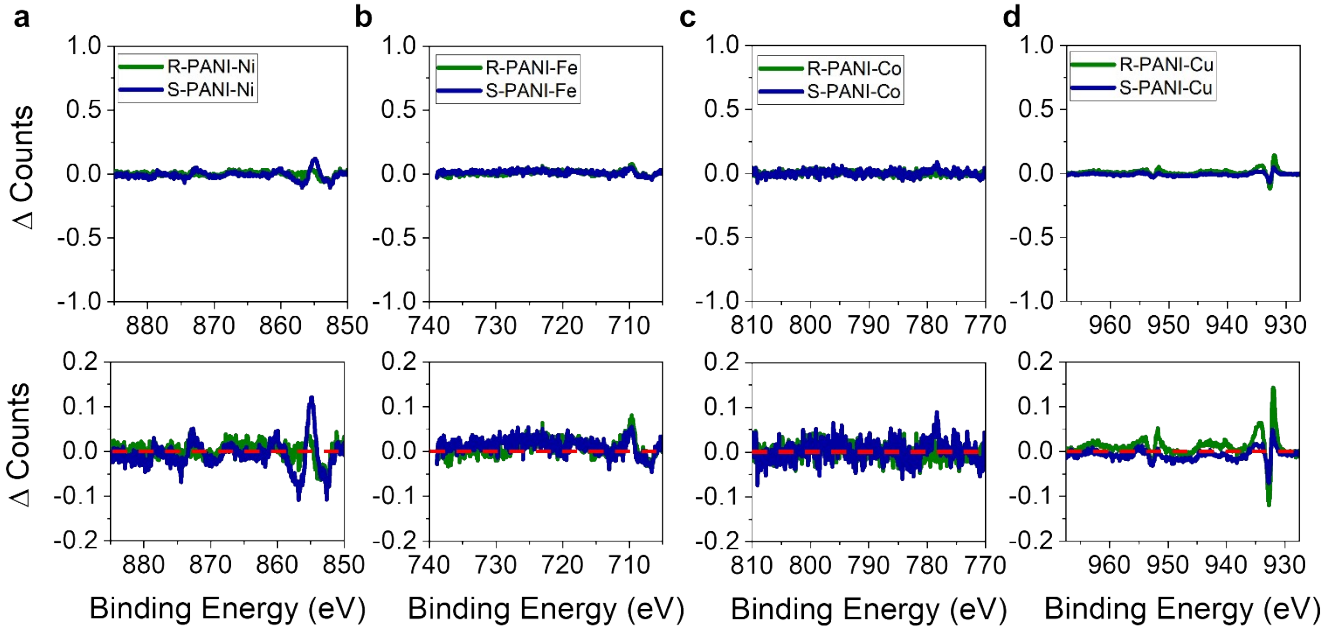

Figure S6. Difference in counts, normalized to the peak maximum of the most intense peak, between chiral-PANI to rac-PANI for the four different catalysts; Ni2p (**a**), Fe2p (**b**), Co2p (**c**), and Cu2p (**d**). The top panel plots the maximum possible difference that could be observed and the bottom panel is zoomed in 5x. The red dashed line at Δ Counts = 0 is a guide to the eye.

Figure S7 shows scanning electron microscopy (SEM) images of rac-PANI (top), S-PANI (middle), and R-PANI (bottom) with electrodeposited nickel (**a**), iron (**b**), cobalt (**c**), and copper (**d**). The images shown indicate that both chiral and racemic systems have similar morphology after electrodeposition of each of the catalysts.

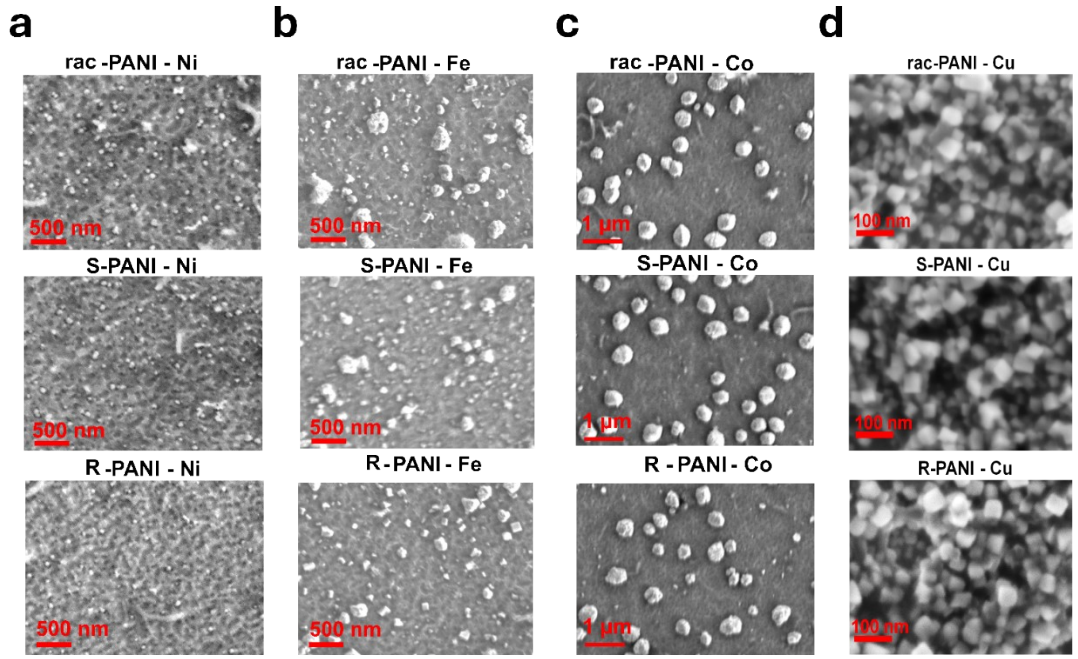

Figure S7 SEM images of PANI- nickel (**a**), iron (**b**), cobalt (**c**), and copper (**d**) on a 10 nm gold coated quartz substrate.

Figure S8 shows representative linear sweep voltammograms in 1M KOH of electrodeposited catalysts and drop cast catalyst ink solutions on R-PANI (solid line) and rac-PANI (dotted line) coated electrodes. A similar improvement to that shown for catalysts on S-PANI compared to rac-PANI is observed.

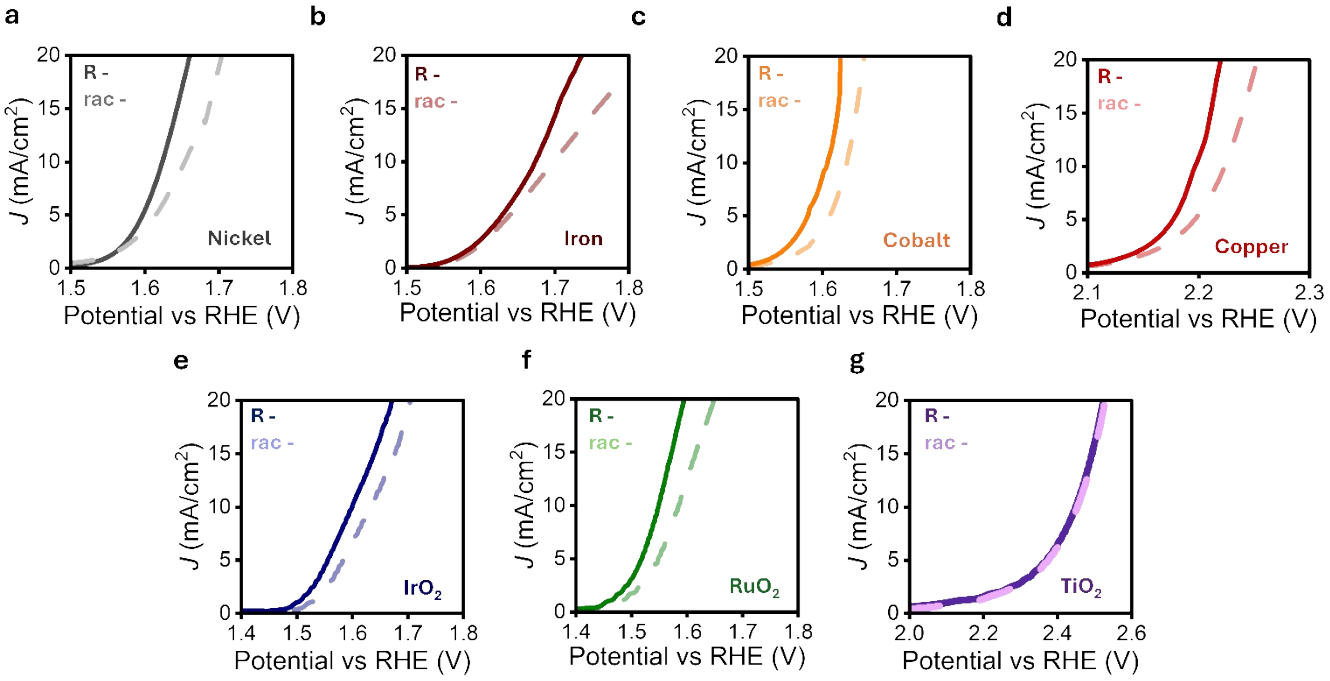

Figure S8 Linear sweep voltammograms of nickel (**a**), iron (**b**), cobalt (**c**), and copper (**d**) electrodeposited catalysts and IrO_2 (**e**), RuO_2 (**f**), and TiO_2 (**g**) drop-casted ink solutions on R-PANI (solid line) and rac-PANI films (dashed line). These data represent the average of three separately prepared electrodes.

Figure S9 shows representative Tafel plots in 1M KOH of electrodeposited catalysts (top row) and drop cast catalyst ink solutions (bottom row) on R-PANI (filled symbols) and rac-PANI (open symbols).

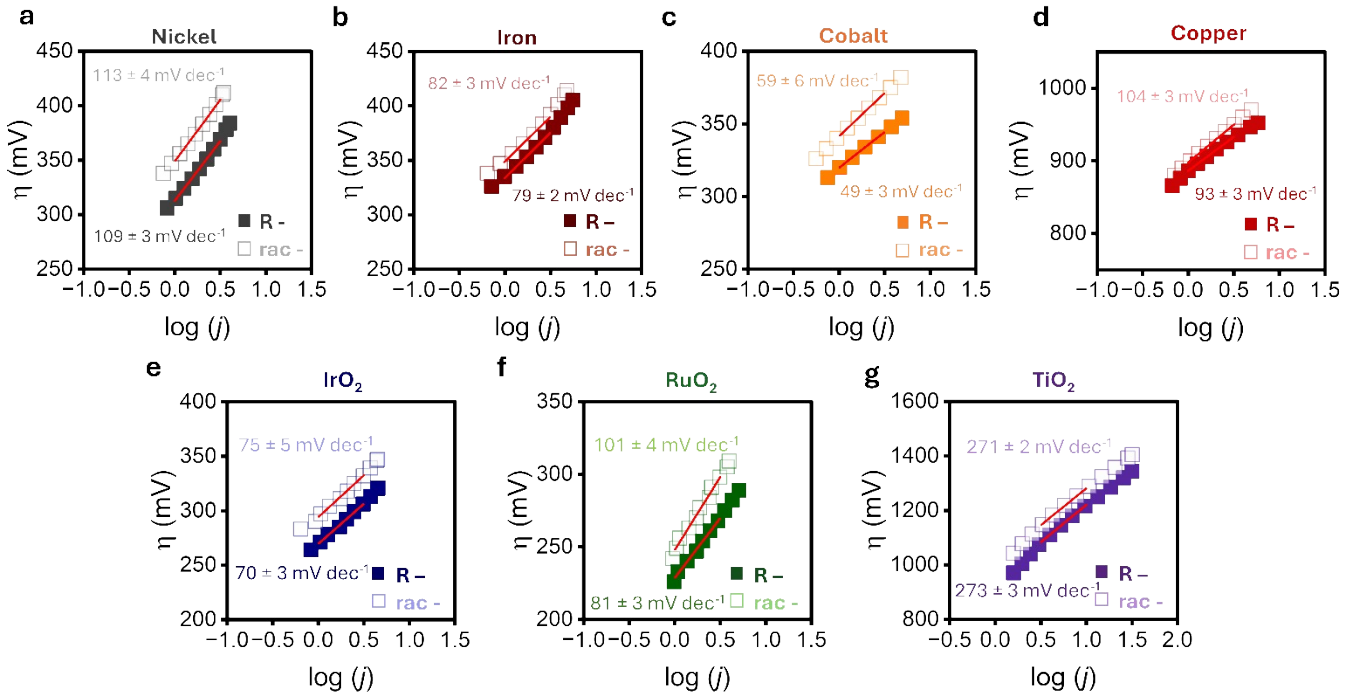

Figure S9 Tafel plots of nickel (**a**), iron (**b**), cobalt (**c**), and copper (**d**) electrodeposited catalysts and IrO_2 (**e**) RuO_2 (**f**), and TiO_2 (**g**)drop casted ink solutions on R-PANI (solid symbol) and rac-PANI films (open symbol). These data represent the average from three separately prepared electrodes and the error in slope is associated with the standard deviation of the mean.

Figure S10 shows representative linear sweep voltammograms in 1M KOH of electrodeposited catalysts and drop cast catalyst ink solutions on S-PANI (blue) and R-PANI (green) coated electrodes. Similar OER activity is observed for the two different types of PANI which further illustrates that there is not a spin-preference for improving reaction effeciency, only that spin alignment at the catalyst surface is occuring.

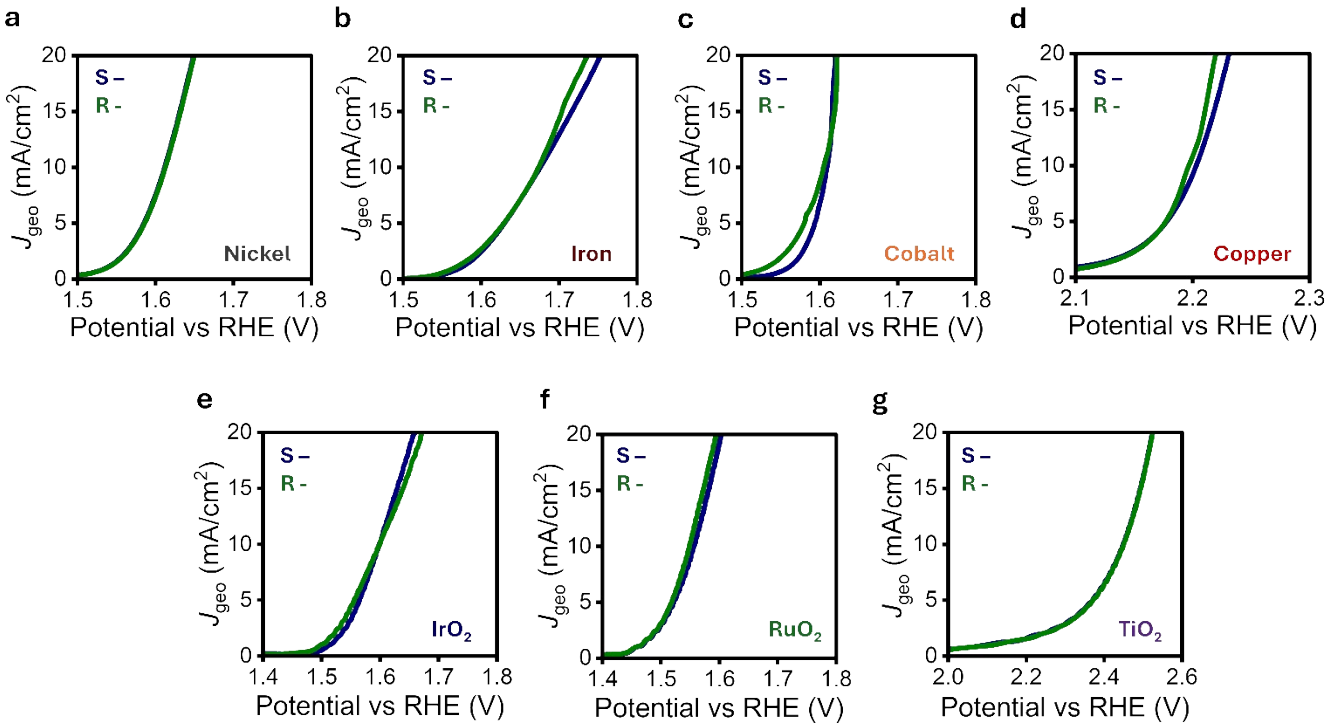

Figure S10 Linear sweep voltammograms of nickel (**a**), iron (**b**), cobalt (**c**), and copper (**d**) electrodeposited catalysts and IrO_2 (**e**), RuO_2 (**f**), and TiO_2 (**g**) drop-casted ink solutions on S-PANI (blue) and R-PANI films (green). These data represent the average of three separately prepared electrodes.

Figure S11 shows representative double layer capacitance measurements from 10 to 70 mV s^{-1} of different catalysts electrodeposited or drop-casted onto S-PANI (blue), rac-PANI (purple), and R-PANI (green). Since the non-Faradaic region of the voltammograms at which the double layer capacitance can be measured coincides with a more resistive form of PANI the absolute ECSA can be skewed. Conversely, the similar slopes for catalysts deposited on chiral (S-, R-) PANI films versus rac-PANI films imply that the electrochemical surface area (ECSA) is within error.

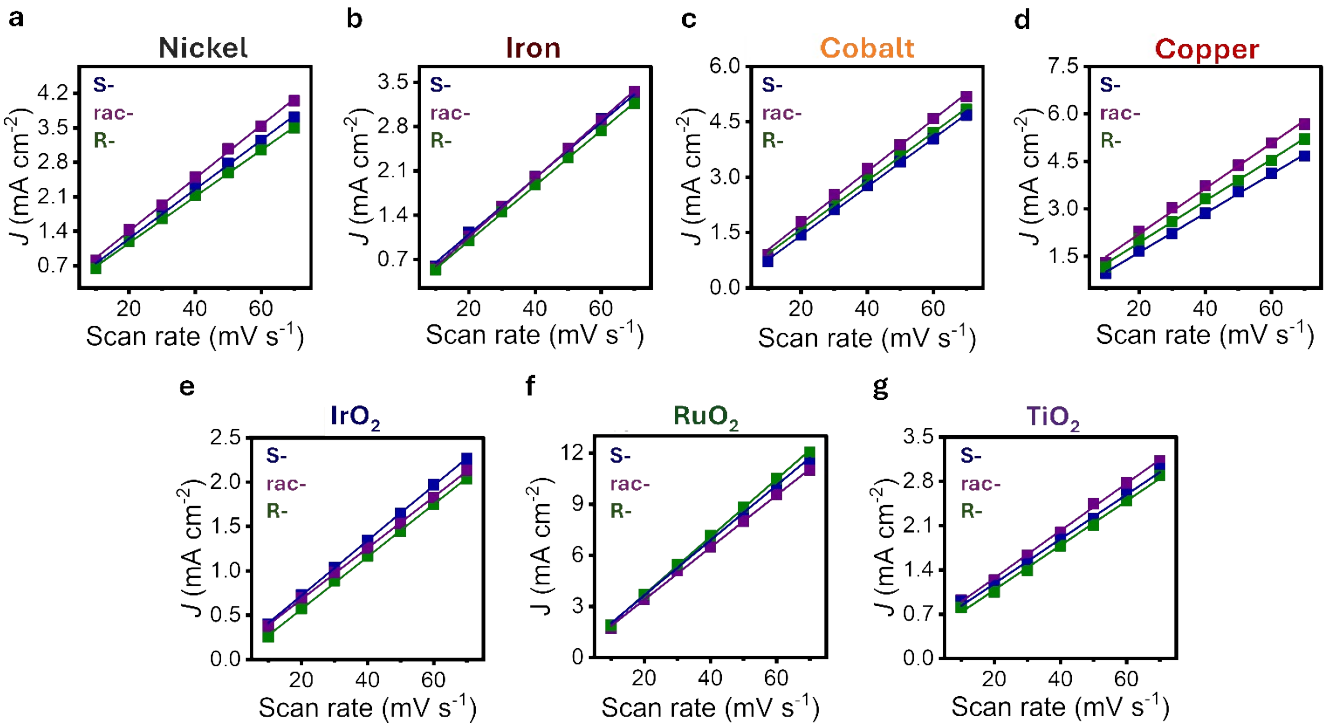

Figure S11 Representative double layer capacitance measurements of nickel (**a**), iron (**b**), cobalt (**c**), copper (**d**) electrodeposited catalysts, and IrO_2 (**e**), RuO_2 (**f**), and TiO_2 (**g**) drop-casted ink solutions on S- (blue), rac- (purple) and R- (green) PANI films. The solid line is a linear fit to the data.

Figure S12 shows linear sweep voltammograms of electrodeposited Ni (**a**) and Co (**b**) catalysts on S-PANI (solid line) and rac-PANI (dashed line) thin films. The peak at ~1.35 V vs RHE for nickel and 1.15 V vs RHE cobalt corresponds to oxidation from M^{2+} to M^{3+} and occurs prior to the OER. The presence of these peaks is consistent with the notion that oxyhydroxides are the primary form of the catalyst during OER.[3, 4] Moreover, the similar area under the oxidation peaks between S- and rac-PANI films demonstrates that the catalyst loadings are essentially the same.

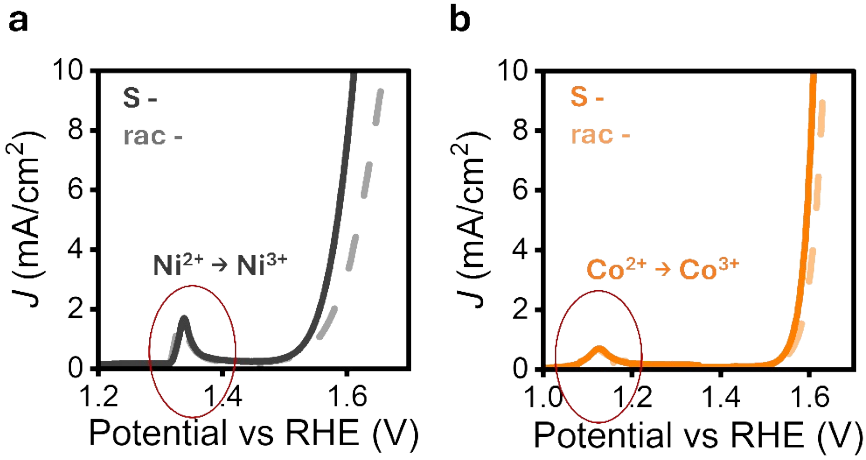

Figure S12 Linear sweep voltammograms of nickel (**a**) and cobalt (**b**) electrodeposited catalysts on S-PANI (solid line) and rac-PANI films (dashed line) in 1M KOH. The oxidation peak of the metal is indicated by a red circle.

Table S1 shows the average *iR* compensation applied for electrodeposited and drop casted catalysts on S-, R-, and rac-PANI films. The similarity in compensated resistance for a given catalyst further suggests the similarity between materials deposited on the different types of PANI.

Table S1. The average and standard deviation of compensated resistance applied during LSV and Tafel data acquisition in Figures 2, 3, S8, & S9

Catalyst	S-PANI (Ω)	R-PANI (Ω)	rac-PANI (Ω)
Nickel	26 ± 4	28 ± 3	26 ± 2
Iron	28 ± 3	26 ± 2	27 ± 3
Cobalt	27 ± 2	26 ± 3	25 ± 3
Copper	28 ± 5	29 ±3	26 ± 2
IrO_2	11 ± 2	11 ± 1	10 ± 1
RuO_2	11 ± 3	12 ± 2	11 ± 2
TiO_2	9 ± 1	9 ± 2	9 ± 1

References

[1] D. Hetemi, V. Noël, J. Pinson, *Biosens. J.*, 2020, **10**, 4.

[2] M. C. Biesinger, B. P. Payne, A. P. Grosvenor, L. W. M., Lau, A. R. Gerson, R. St. C. Smart, *Appl. Surf. Sci.*, 2011, **257**, 2717-2730.

[3] O. Diaz-Morales, D. Ferrus-Suspedra, M. T. Koper, *Chem. Sci*., 2016, **7**, 2639-2645.

[4] M. S. Burke, M. G. Kast, L. Trotochaud, A. M. Smith, S. W. Boettcher, *J. Am. Chem. Soc*., 2015, **137**, 3638-3648.